

Cite this: DOI: 00.0000/xxxxxxxxxx

Nonadiabatic forward flux sampling for excited-state rare events[†]

Madlen Maria Reiner,^{ab} Brigitta Bachmair,^{ac} Maximilian Xaver Tiefenbacher,^{ac} Sebastian Mai,^d Leticia González,^{*ad} Philipp Marquetand,^{*ad} and Christoph Dellago^{*ae}

Received Date

Accepted Date

DOI: 00.0000/xxxxxxxxxx

We present a rare event sampling scheme applicable to coupled electronic excited states. In particular, we extend the forward flux sampling (FFS) method for rare event sampling to a nonadiabatic version (NAFFS) that uses the trajectory surface hopping (TSH) method for nonadiabatic dynamics. NAFFS is applied to two dynamically relevant excited-state models that feature an avoided crossing and a conical intersection with tunable parameters. We investigate how nonadiabatic couplings, temperature, and reaction barriers affect transition rate constants in regimes that cannot be otherwise obtained with plain, traditional TSH. The comparison with reference brute-force TSH simulations for limiting cases of rareness shows that NAFFS can be several orders of magnitude cheaper than conventional TSH, and thus represents a conceptually novel tool to extend excited-state dynamics to time scales that are able to capture rare nonadiabatic events.

1 Introduction

Chemical reactions initiated by the absorption of a photon are at the core of organic synthesis,¹ catalysis,² optogenetics,³ protein modification,⁴ the conversion and storage of solar energy,⁵ and hold promise for many other applications.⁶ While many photochemical reactions are ultrafast and occur on a femtosecond time scale,⁷ high barriers on electronically excited potential energy surfaces (PEs) or nonadiabatic transitions⁸ with small couplings may lead to much slower reactions. For instance, the average reaction time for the keto-enol tautomerism of 2-benzylbenzophenone is half a millisecond,^{9,10} *i.e.*, many orders of magnitude longer than the time scale of basic molecular motions. The resulting separation of time scales represents a huge challenge for the computer simulation of such rare reactive events. In particular, the femtosecond time step¹¹ needed to accurately capture nuclear dynamics^{12,13} makes it unfeasible to simulate rare

photoreactions using straightforward quantum dynamics^{14,15} or nonadiabatic mixed quantum-classical molecular dynamics,^{16,17} even if recently developed machine learning approaches bring such simulations from the picosecond¹⁸ to the nanosecond time scale.^{19–22}

For classical dynamics in the electronic ground state, numerous computational methods have been developed to address the rare event problem,¹² including umbrella sampling,²³ blue-moon sampling,²⁴ steered MD,²⁵ hyperdynamics,²⁶ milestone-ing,²⁷ metadynamics,²⁸ the string method,²⁹ transition path sampling (TPS),³⁰ and forward flux sampling (FFS).^{31–33} The investigation of rare events in excited-state problems, however, is much less explored. Recent efforts relied on metadynamics to probe intersection crossing points between adiabatic electronic states that lead to the slow formation of photoproducts.^{34–36} In other work, TPS was used to sample the nonadiabatic dynamics of open quantum systems as described by a quantum master equation preserving detailed balance.³⁷ TPS has also been applied to semiclassical pathways³⁸ obtained by trajectory surface hopping (TSH).³⁹ In contrast to other rare event methods, TPS does not require any prior knowledge of the reaction mechanism in terms of a reaction coordinate. The backward propagation of trajectories required in TPS, however, is not possible in the framework of TSH.⁴⁰ While this difficulty can be circumvented by generating reverse trajectories with approximate quantum weights and subsequently reweighting them,^{38,41} this procedure reduces the efficiency of the TPS simulation.

In this paper, we show how rare but important events occurring

^a Research Platform on Accelerating Photoreaction Discovery (ViRAPID), University of Vienna, Währinger Straße 17, 1090 Vienna, Austria. E-mail: leticia.gonzalez@univie.ac.at, philipp.marquetand@univie.ac.at, christoph.dellago@univie.ac.at

^b Vienna Doctoral School in Physics, University of Vienna, Boltzmannngasse 5, 1090 Vienna, Austria.

^c Vienna Doctoral School in Chemistry, University of Vienna, Währinger Straße 42, 1090 Vienna, Austria.

^d Institute of Theoretical Chemistry, Faculty of Chemistry, University of Vienna, Währinger Straße 17, 1090 Vienna, Austria.

^e Faculty of Physics, University of Vienna, Kolingasse 14-16, 1090 Vienna, Austria.

[†] Electronic Supplementary Information (ESI) available: See DOI: 00.0000/00000000.

in electronic excited states can be studied with FFS, a trajectory based approach originally developed for driven non-equilibrium stochastic systems with unknown stationary phase space distribution. In this approach, a sequence of non-intersecting interfaces between reactants and products is used to sample the ensemble of transition paths and calculate reaction rate constants. We combine the FFS methodology with TSH dynamics, exploiting that FFS requires only forward integration of the equations of motion. Hence, it is not affected by the lack of time reversal symmetry of TSH. As demonstrated using two simple illustrative models, the novel nonadiabatic FFS (NAFFS) method presented here provides a general approach for enhanced path sampling in electronic excited states and allows studying rare nonadiabatic reactions on time scales exceeding by far those accessible with brute-force TSH simulations.

The remainder of the paper is organized as follows. In Sec. 2 we lay out the FFS algorithm and describe how it is combined with TSH. Details on the implementation of the method are provided in Sec. 3. Results obtained for two simple model systems are presented and discussed in Sec. 4 and conclusions are provided in Sec. 5.

2 Theory

In the following, we review the main concepts behind the FFS method and the TSH algorithm and explain how they had to be extended in order to be combined into NAFFS.

2.1 Forward flux sampling of rare events in electronically excited states

Rare event sampling methods for ground state problems sample regions of the phase space that are unlikely to be visited by standard MD calculations. Among them, TPS approaches sample fully dynamical trajectories, (*i.e.*, trajectories which could occur in exactly the same way in brute-force MD simulations with the correct probability) with Monte Carlo methods acting in path space (*i.e.*, trajectory space).¹² In these algorithms, transition paths—*i.e.*, rare trajectories that start in the initial reactant region of phase space and end in the final product region of phase space—are sampled by generating a new trajectory from a given trajectory, typically by propagating the system both forward and backward in time. The newly generated trajectory is then accepted or rejected according to a criterion guaranteeing that the trajectories follow the statistics dictated by the transition path ensemble. In this way, reactivity is maintained at all times during the TPS simulation and no computing resources are wasted to follow the dynamics of the system during the long periods when no transition occurs. Analysis of the sampled transition paths then provides insights into the underlying reaction mechanisms.³⁰ In transition interface sampling,⁴² a variant of TPS, ensembles of pathways that cross a sequence of interfaces between reactant and product regions are considered. This procedure significantly enhances the sampling of transition paths and uses the rejected trajectories ingeniously to calculate reaction rate constants.

As most other TPS methods, also transition interface sampling relies on the time reversibility of the dynamics and on explicit

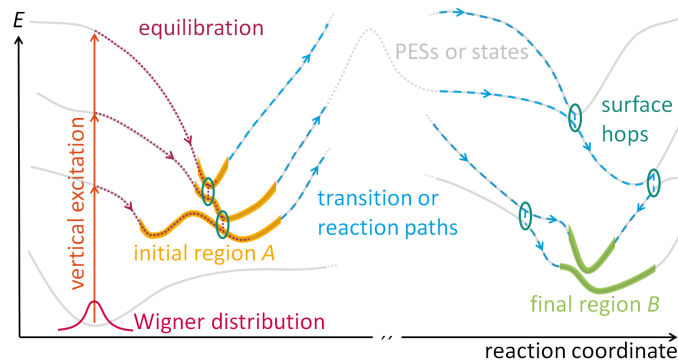


Fig. 1 Schematic illustration of a nonadiabatic PES landscape, showing a possible definition of the initial and final regions *A* and *B*. In the framework of a typical TSH simulation, a nuclear ensemble of vertically excited configurations drawn from the Wigner distribution relaxes into one or several minima included in *A* (equilibration), which serves as starting region for the NAFFS simulation. NAFFS then samples reaction paths that connect *A* and *B* including rare events in electronic excited states (*e.g.*, an energy barrier). Due to the nonadiabatic nature of the PES landscape, surface hops (circles) between states can happen during the dynamics.

knowledge of the stationary phase space distribution. Hence, the application of TPS methods to irreversible non-equilibrium systems is not straightforward. This difficulty motivated the development of FFS,^{31–33,43} a simulation method for rare events in which the equations of motion are integrated only forward in time such that it does not suffer from lack of knowledge of the stationary distribution and the absence of microscopic reversibility. Hence, FFS, a splitting method based in spawning swarms of trajectories connecting interfaces, can be applied to study rare events occurring in non-equilibrium systems.^{43,44} These properties make FFS ideally suited for combining it with TSH, which does not satisfy detailed balance and generally produces an unknown stationary distribution.

As it is customary in FFS, we consider systems that undergo a rare transition from an initial reactant region of phase space called *A* to a final product region called *B*. Both regions, *A* and *B*, are supposed to be stable, meaning that the system resides in them for long times compared to the time where it is in an unstable region, *e.g.*, when it undergoes a transition from *A* to *B*.¹² Both regions are defined in terms of collective variables, that is, functions of the phase space coordinates, *e.g.*, bond lengths, angles, or dihedrals.⁴⁵ What distinguishes our application of FFS from others is the novelty that we explicitly include one or several PESs in the definition of our initial and final regions (see Fig. 1); this is necessary to study nonadiabatic excited-state reactions. Throughout this work, we use the term “region” for stable phase space regions in the FFS context, and the term “transition path” as a synonym of “reaction path” to describe the evolution of the system between regions. We use the term “state” for electronic states or PESs, and the term “hop” to describe nonadiabatic changes between states. Hence, in our nonadiabatic setting, one or several states can be part of the definition of a region, and a transition path between regions can include hops between electronic states.

A typical TSH simulation begins with an instantaneous vertical excitation (that mimics the absorption of a photon) of a nuclear ensemble of geometrical configurations, *e.g.*, drawn from a Wigner distribution in the electronic ground state minimum (see Fig. 1 left).¹⁷ In excited-state reactions involving rare events, after the vertical excitation the system would evolve (see dark red dotted equilibration trajectories in Fig. 1) into a stable excited-state region *A*, in which it stays for a very long time before the rare event occurs and the system transitions to the final region *B* (see blue dashed transition paths in Fig. 1). To ensure the greatest possible generality in the choice of reaction pathways, the stable excited-state region *A* may span several PESs, where the different configurations of the nuclear ensemble land after equilibration. Further, the initial region *A* is flexible enough to include different regions of a single PES, if needed. Likewise, the final region *B* (see green PESs parts in Fig. 1) can expand over multiple states. For simplicity, neither the vertical excitation process nor the equilibration to the initial region *A* is included in our NAFFS algorithm but can be performed with standard initial condition and TSH simulations.

As the transition interface sampling method,⁴² FFS is an interface-based approach⁴⁶ where interfaces λ_i (*i.e.*, intermediate stages between the regions *A* and *B*) are defined in terms of collective variables. There exist several approaches to the proper placement of the interfaces.^{47–50} In NAFFS, the interfaces are also able to include a range of PESs, as the initial and final regions do. For the applications presented later, we define the first and last interfaces to equal the boundaries of the stable regions *A* and *B*, *i.e.*, $\lambda_A \equiv \lambda_0$ and $\lambda_B \equiv \lambda_{n+1}$, as often done so.³³ The rate constant k_{AB} is then calculated as³¹

$$k_{AB} = \phi_A P_A(\lambda_{n+1}|\lambda_0) = \phi_A \prod_{i=0}^n P_A(\lambda_{i+1}|\lambda_i), \quad (1)$$

where ϕ_A is the effective positive flux out of *A* through the boundary of *A*, and $P_A(\lambda_j|\lambda_i)$ is the probability of a trajectory that started in *A* crossing the interface λ_j in the direction of *B* given that it has already crossed the interface λ_i . There are two common ways to calculate the flux ϕ_A through the boundary of the initial region *A*. The first⁴⁹ involves running an MD simulation in region *A* and counting the number of times N_0 that the interface λ_0 is crossed in the outward direction of *A* divided by the simulation time (see Fig. 2a). Here it is assumed that the trajectory does not enter the final product region *B* during the MD simulation, or if it does, it is immediately reset to *A* and re-equilibrated.³² Alternatively, only for equilibrium systems and reversible reactions and if the trajectory visits both regions *A* and *B* several times in the MD run, the flux ϕ_A can be calculated by dividing the number N_0 by the time $T_{\mathcal{A}}$ the system has spent in the overall region \mathcal{A} during the simulation,⁴²

$$\phi_A = \frac{N_0}{T_{\mathcal{A}}}. \quad (2)$$

The time $T_{\mathcal{A}}$ spent in the overall region \mathcal{A} is not only the time the trajectory is located in region *A*, but also the time spent outside *A* as long as *B* is not reached. If the trajectory enters *B*, $T_{\mathcal{A}}$ resumes counting after the trajectory exits *B* and re-enters *A*. Provided

that both approaches to calculate the flux ϕ_A are applicable, one or the other could be computationally more efficient and which one to take is decided depending on the system to study.

The crossing probabilities $P_A(\lambda_{i+1}|\lambda_i)$ are given by the fraction of accepted Monte Carlo moves or “shots” that are initiated on the shooting interface λ_i and cross the subsequent interface λ_{i+1} with respect to the total number M of trial shots initiated from λ_i . In the first FFS cycle, the shooting points on the boundary λ_0 of the initial region *A* are randomly chosen from the N_0 crossing points collected in the flux simulation, exploiting the fact that due to the underlying stochastic dynamics of the system (induced typically by a thermostat), two shots beginning in the same point produce different trajectories (see Fig. 2b). Final points of accepted shots in each FFS cycle serve as possible shooting points for the next FFS cycle (see Fig. 2c).³² Final reactive paths (see Fig. 2d) are obtained in accordance to their correct weight in the transition path ensemble, *i.e.*, the relative probabilities of transition paths with respect to the considered system, and, hence, those of reactive paths obtained in MD simulations are conserved.⁵¹ In summary, the difficult problem of finding a reaction coordinate and a phase space probability distribution is replaced by the (usually) simpler task of defining reactant and product regions *A* and *B*, and interfaces in between.

The relative error of the rate constant k_{AB} obtained in an FFS simulation can be estimated as^{33,49,52}

$$\frac{\Delta k_{AB}}{k_{AB}} = \sqrt{\frac{1}{N_0} + \sum_{i=0}^n \frac{1 - P_A(\lambda_{i+1}|\lambda_i)}{P_A(\lambda_{i+1}|\lambda_i) \cdot M_i}}, \quad (3)$$

where Δk_{AB} is the standard deviation of the calculated rate constant k_{AB} , and M_i is the number of shots performed starting from shooting points on interface λ_i . The relative error estimation given by Eq. (3) corresponds to a Gaussian error propagation, taking into consideration an estimate of the relative error of the flux ϕ_A as

$$\frac{\Delta \phi_A}{\phi_A} = \frac{\sqrt{N_0}}{N_0}, \quad (4)$$

and the estimated errors of the crossing probabilities obtained for each shooting interface as

$$\Delta P_A(\lambda_{i+1}|\lambda_i) = \sqrt{\frac{P_A(\lambda_{i+1}|\lambda_i) \cdot (1 - P_A(\lambda_{i+1}|\lambda_i))}{M_i}}. \quad (5)$$

2.2 Stochastic excited-state molecular dynamics simulations using trajectory surface hopping

The application of the FFS method requires an MD algorithm to propagate the system in time. Here, we use a velocity Verlet-type^{53–55} algorithm with Langevin dynamics in combination with the surface hopping including arbitrary couplings (SHARC) approach.^{56–58} SHARC is an extension of Tully’s fewest switches⁵⁹ TSH method, able to describe on the same footing internal conversion between states of the same spin multiplicity via nonadiabatic couplings and intersystem crossing between states of different spin multiplicity via spin-orbit couplings.

As a TSH method, SHARC is a mixed quantum-classical simulation technique, where the nuclei are considered classical particles

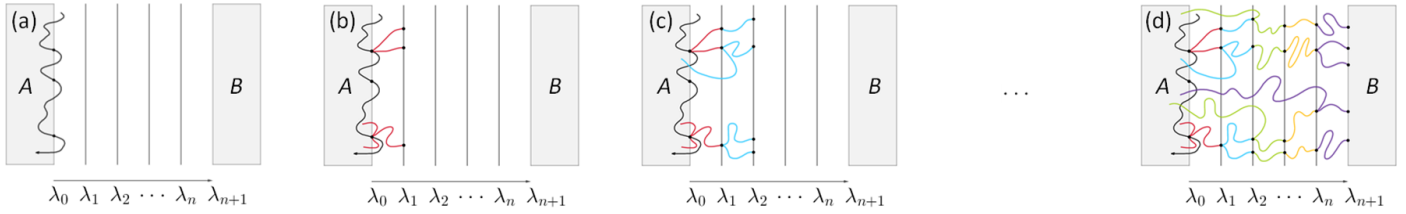


Fig. 2 The working principle of the forward flux sampling scheme.⁴³ (a) A brute-force MD simulation in the initial reactant region A is performed and the snapshots where the trajectory exits A are stored as initial shooting points. (b) Shots of randomly chosen initial shooting points are either rejected if they enter A , or accepted if they cross the adjacent interface λ_1 . Due to the underlying stochastic dynamics, trajectories initiated in the same shooting point differ. Crossing snapshots are stored as shooting points for the next FFS cycle. (c) In the second FFS cycle, randomly chosen trajectories ending in shooting points on the interface λ_1 are continued, and either accepted if they cross the next adjacent interface, or rejected if they enter A . This procedure is repeated for all interfaces λ_i . (d) Once the last FFS cycle is finished, final transition paths from A to B are obtained by piecing together the accepted partial paths obtained in each FFS cycle.

and nonadiabatic effects are accounted for by including multiple PESs.⁶⁰ Nuclei always follow the force corresponding to one single PES (the “active state”), and instantaneous hops between adiabatic PESs mimic nonadiabatic changes, according to hopping probabilities based on the quantum mechanical evolution of the electronic populations of the different states.⁵⁸ As the TSH algorithm treats the electrons quantum mechanically, it solves the electronic time-dependent Schrödinger equation⁵⁷

$$i\hbar \frac{d}{dt} |\Psi\rangle = \hat{H} |\Psi\rangle, \quad (6)$$

where \hat{H} is the electronic Hamilton operator, \hbar the reduced Planck constant, and $|\Psi\rangle$ the electronic wave function, which in a linear combination of basis states ψ_α is written in terms of the coefficients c_α ,

$$|\Psi\rangle = \sum_{\alpha} c_{\alpha} |\psi_{\alpha}\rangle. \quad (7)$$

Combining Eq. (6) and Eq. (7) yields the equations of motion for the electronic population vector \mathbf{c} consisting of the electronic wave function coefficients c_α ,

$$\frac{d}{dt} \mathbf{c} = - \left[\frac{i}{\hbar} H + K \right] \mathbf{c} \quad (8)$$

with coupling matrix K and Hamilton matrix H .

SHARC uses a fully “adiabatic” or diagonal representation in the propagation.^{56,57} In the simulations presented in this work, the coefficients c_α are propagated as⁵⁸

$$\mathbf{c}(t + \Delta t) = R(t + \Delta t, t) \cdot \mathbf{c}(t) \quad (9)$$

with time step Δt . The corresponding propagator matrix R is given as

$$R(t + \Delta t, t) = S(t, t + \Delta t)^\dagger \prod_{i=1}^s R_i, \quad (10)$$

with

$$R_i = \exp \left[-\frac{i}{\hbar} H_i \Delta \tau \right], \quad (11)$$

and

$$H_i = H(t) + \frac{i}{s} \left(S(t, t + \Delta t) H(t + \Delta t) S(t, t + \Delta t)^\dagger - H(t) \right), \quad (12)$$

where s the number of substeps with length $\Delta \tau = \frac{\Delta t}{s}$ within

a time step of length Δt , and overlap matrix S calculated by $S(t, t + \Delta t) = U^\dagger(t) \cdot U(t + \Delta t)$ from transformation matrices U obtained by diagonalizing the diabatic Hamiltonian, $H = U^\dagger H^{\text{diab}} U$ at times t and $t + \Delta t$. The overlap matrix and Hamiltonian are phase-corrected⁵⁸ in each time step to avoid random changes in the population transfer direction because of random phases of the transformation matrices U . The hopping probabilities, *i.e.*, the probabilities to hop from the current or active state β to a different state α , are given by⁵⁷

$$P_{\beta \rightarrow \alpha} = \left(1 - \frac{|c_\beta(t + \Delta t)|^2}{|c_\beta(t)|^2} \right) \frac{\Re \left[c_\alpha(t + \Delta t) R_{\alpha\beta}^* (c_\beta(t))^* \right]}{|c_\beta(t)|^2 - \Re \left[c_\beta(t + \Delta t) R_{\beta\beta}^* (c_\beta(t))^* \right]}, \quad (13)$$

with electronic coefficients in state α and β , namely c_α and c_β , and complex conjugated elements of the propagator matrix R . A surface hop to state $\tilde{\alpha}$ is attempted only if a random number r drawn from a uniform distribution in the interval $[0, 1]$ satisfies⁶¹

$$\sum_{i=1}^{\tilde{\alpha}-1} P_{\beta \rightarrow i} < r \leq \sum_{i=1}^{\tilde{\alpha}} P_{\beta \rightarrow i}. \quad (14)$$

If the total energy of the system is smaller than the potential energy of the envisaged new state $\tilde{\alpha}$, no hop is performed and the system stays in the state β , *i.e.*, the new active state β is the same as the old state—this is called a “frustrated hop”. Otherwise, if the potential energy $E_{\tilde{\alpha}}$ of the envisaged new state $\tilde{\alpha}$ is smaller than or equal to the system’s total energy E_{total} , a surface hop $\beta \rightarrow \tilde{\alpha}$ is performed. As in most TSH implementations, during the surface hop the total energy is kept constant by rescaling the nuclear velocities \mathbf{v} . By default in SHARC, this is done according to the scheme¹⁷

$$\mathbf{v}' = \sqrt{\frac{E_{\text{total}} - E_{\tilde{\alpha}}}{E_{\text{kin}}}} \cdot \mathbf{v}, \quad (15)$$

where E_{kin} is the total kinetic energy before the hop, *i.e.*, the rescaled velocity vector \mathbf{v}' is parallel to the original one, \mathbf{v} . After this adjustment, the state $\tilde{\alpha}$ is the new active state β of the system. Other velocity adjustment varieties are available in SHARC.⁶²

In TSH, electronic populations in the non-active states α follow the forces of the active state β , even though in a proper quantum mechanical description they should follow the forces of their respective state α . This problem is known as “overcoher-

ence”,^{16,17,63} and in the present work is accounted for by modifying the electronic coefficients of the states α according to the energy difference to the active state β after the surface hopping procedure,⁶⁴

$$c'_\alpha = c_\alpha \cdot \exp \left[-\frac{1}{2} \Delta t \frac{|E_\alpha - E_\beta|}{\hbar} \left(1 + \frac{C}{E_{\text{kin}}} \right)^{-1} \right], \quad \alpha \neq \beta, \quad (16)$$

$$c'_\beta = \frac{c_\beta}{|c_\beta|} \left(1 - \sum_{\alpha \neq \beta} |c'_\alpha|^2 \right)^{-\frac{1}{2}}$$

with decoherence parameter C .

Although TSH algorithms already have an intrinsically stochastic character due to the randomness of the hops, their degree of stochasticity is not sufficient for an application of the FFS algorithm, especially in regions away from probable hopping points. These regions are characterized by large energy gaps between adjacent PESs. To increase the level of stochasticity beyond random hops in a controllable way, we consider a system evolving under the influence of friction and random forces as described by the Langevin equation

$$m\dot{\mathbf{v}} = -\gamma\mathbf{v}(t) - \nabla E(\mathbf{x}(t)) + \boldsymbol{\eta}(t). \quad (17)$$

Here, \mathbf{x} denotes the positions of all atoms, E is the potential energy, m the mass and γ the friction constant controlling the magnitude of the frictional forces, which are proportional to the velocities. In the above equation, $\boldsymbol{\eta}(t)$ denotes Gaussian white noise with zero mean, $\langle \boldsymbol{\eta}(t) \rangle = 0$, and delta-like correlations $\langle \boldsymbol{\eta}(t) \boldsymbol{\eta}(t') \rangle = 2\gamma k_B T \Delta t \delta(t - t')$ with Boltzmann’s constant k_B and temperature T . The Langevin equation can be viewed as resulting from coupling the system to a heat bath with temperature T that causes friction and random forces related by the fluctuation-dissipation theorem. The strength of the coupling to the heat bath is controlled by the friction constant γ and for $\gamma = 0$ the Langevin equation reduces to Newton’s equations of motion.

The Langevin equation (17) is solved numerically in small time steps Δt using a velocity Verlet-like integration scheme,⁶⁵

$$\mathbf{x}(t + \Delta t) = \mathbf{x}(t) + b\mathbf{v}(t)\Delta t - \frac{b}{2m}\nabla E(\mathbf{x}(t))\Delta t^2 + \frac{b}{2m}\boldsymbol{\xi}(t)\Delta t,$$

$$\mathbf{v}(t + \Delta t) = a\mathbf{v}(t) - \frac{\Delta t}{2m}[a\nabla E(\mathbf{x}(t)) + \nabla E(\mathbf{x}(t + \Delta t))] + \frac{b}{m}\boldsymbol{\xi}(t + \Delta t), \quad (18)$$

where $b = \left(1 + \frac{\gamma\Delta t}{2m}\right)^{-1}$, and $a = \left(1 - \frac{\gamma\Delta t}{2m}\right)\left(1 + \frac{\gamma\Delta t}{2m}\right)^{-1}$. In the above equations, $\boldsymbol{\xi}(t)$ and $\boldsymbol{\xi}(t + \Delta t)$ denote independent Gaussian random numbers with zero mean and variance $2\gamma k_B T \Delta t$.

This methodology allows SHARC simulations to follow stochastic dynamics and is, therefore, ideally suited for combination with the FFS algorithm.

3 Implementation

The practical implementation of NAFFS relies on two program suites. On the TSH side, we extended SHARC^{56–58} with a Langevin thermostat to endow the dynamics with the stochastic

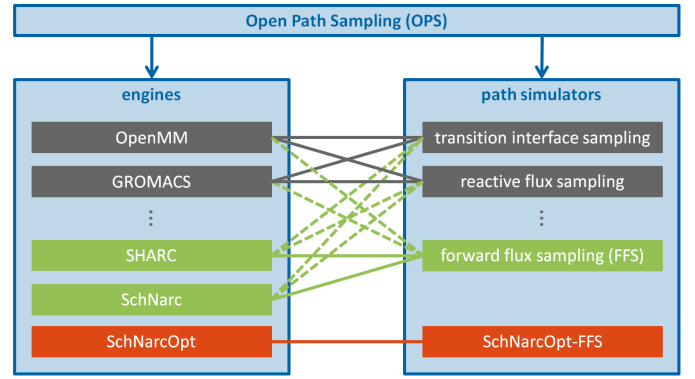


Fig. 3 Architecture of the OPS library. Examples of existing engines, simulators, and combinations between them are shown in gray. Green boxes indicate new implementations. Dashed green lines indicate new possible combinations of engines and simulators and solid lines explicit new implementations of NAFFS. A dedicated SchNarcOpt engine tailored to a new FFS implementation SchNarcOpt-FFS for computational efficiency is highlighted in red.

ity required for FFS (Sec. 2.2). On the FFS side, we used Open Path Sampling (OPS),^{66,67} a Python library for path sampling simulations capable to work with various MD codes. For example, OPS is interfaced with two popular MD engines: OpenMM^{68,69} and GROMACS^{70,71} (see gray engines in Fig. 3). We have now implemented the SHARC suite and the SchNarc⁷² method via the SHARC driver pySHARC⁷³ as new general engines in OPS, see green engines in Fig. 3. Hence, any quantum chemical method compatible with the SHARC program for computing PESs and electronic properties is now also available for NAFFS simulations. SchNarc was originally developed as an interface between the SHARC program and an extension of the neural network potential SchNet^{74,75} to excited-state properties.⁷² We do not use neural networks in this work, but because SchNarc is not based on file I/O it allows for computationally much more efficient path sampling simulations using TSH dynamics. An additional advantage of the SchNarc engine is that it opens the possibility of using neural network potentials to compute PESs in the future, further decreasing computational costs.

To accompany both engines, SHARC and SchNarc, we implemented an OPS tool to capture snapshots, *i.e.*, individual frames of a trajectory. Such a tool is needed to describe the system at a particular point in time, where specific ranges of PESs are included in addition to the atomic positions and velocities that define the collective variables. Both, the ranges of PESs and collective variables, are used for the definition of the stable initial and final regions A and B as well as the definition of the FFS interfaces. We note that, as usual in OPS, we also include in our engines an additional rejection criterion for discarding trial shots if those exceed a user-given number of time steps. Although this number should be chosen such that (almost) no trajectories are discarded, such implementation is useful, as it aids, for example, the discovery of new stable minima in the region between A and B . From a practical point of view, a rejection criterion is also helpful to avoid very long unnecessary calculations in such a *priori* unknown stable minima by terminating the respective trajectory

calculation and continuing with the next shot.

In OPS any engine can be combined with any TPS simulator, such as transition interface sampling⁴² or reactive flux sampling,⁷⁶ see Fig. 3. As an additional transition path sampling method in the OPS library, here we implemented a general FFS simulator applicable to excited states, see green simulator in Fig. 3.

The advantage of both the general SHARC engines and the general FFS simulator is that they are implemented in the spirit of OPS, *i.e.*, any engine can be combined with any path simulators, so that, in principle, now SHARC (or SchNarc) can be used with any method available in OPS (dashed green lines) and certainly both engines effectively work with FFS (solid green lines). Despite their flexibility, we have also created a dedicated SchNarcOpt engine that is combined with an optimized FFS-SchNarcOpt path simulator (red in Fig. 3), which, although specific, is computationally more efficient since it does not require file I/O. This specific NAFFS implementation has been used in the applications below in order to keep the computational cost as low as possible.

The vertical excitation and the equilibration process (recall Fig. 1) pose a necessary preliminary step prior to any NAFFS simulation. In this work, these steps are carried out in a plain SHARC/SchNarc-TSH simulation. Thus, the workflow of a NAFFS simulation begins with the flux simulation and collection of initial shooting points on the boundary of the initial region *A* (see Fig. 2a). This process is done via the SchNarcOpt engine through OPS and it is followed by the FFS cycles (see Fig. 2b-d), executed via the SchNarcOpt-FFS path simulator in OPS.

In summary, the workflow of a typical NAFFS simulation starts with generating initial conditions (*e.g.*, Wigner sampling and vertical excitation, see Fig. 1), and a relaxation into the initial region, followed by the NAFFS method that generates transition trajectories between the initial and final regions.

To ensure transparency and reproducibility of the obtained results, the code developed is made freely available (see Sec. S1 †).

4 Results and Discussion

As a first application of NAFFS, here we employ two dynamically relevant analytical potential energy landscapes that have been constructed to include rare events in different conditions. We deliberately choose simple analytical models for testing NAFFS rather than a real molecule because they allow for a systematic investigation of different parameters and demonstrate the broad applicability of NAFFS even in extreme situations, regardless of low or high temperature, strong or weak nonadiabaticity. Further, our models can be tuned so that NAFFS results can be compared with reference data obtained with plain brute-force TSH simulations under different conditions. These TSH calculations have been also performed via the SchNarcOpt engine through OPS. The future simulation of real molecules is straightforward, *i.e.*, does not require any further implementation, only investing in the calculation of on-the-fly multidimensional PESs at the desired quantum chemical level of theory.

The first system features an avoided crossing between two states, see Sec. 4.1. Using this model, we demonstrate the es-

sential functionality of NAFFS by calculating the temperature dependence of the transition rate constant with the energy barrier of the avoided crossing. Further, for this model we investigate the influence of nonadiabatic effects on the transition rate constant by varying the gap size between the PESs and thus the rareness of the event.

The second system includes a conical intersection between two states, see Sec. 4.2. This model shows richer nonadiabatic dynamics than the one-dimensional avoided crossing and allows us to focus on the dependence of the reaction rate constant on temperature and to study the contributions of trajectories with different numbers of hops.

Both models demonstrate that NAFFS yields correct results compared to reference plain brute-force TSH simulations in a fraction of the computational time and thus is ideally suited to study general rare nonadiabatic reactions.

4.1 Rare event dynamics through an avoided crossing

We define a three-dimensional potential energy landscape from two diabatic harmonic potentials of the form

$$V_{\pm}(x, y, z) = \frac{\epsilon}{x_0^2} \left((x \pm x_0)^2 + 20y^2 + 20z^2 \right), \quad (19)$$

defined in the Cartesian coordinates x , y , and z . In x -direction the potential is bi-stable with minima at $\pm x_0$ separated by a barrier of height ϵ . The tight harmonic potentials acting on the y and z coordinates make the system effectively one-dimensional along the x coordinate. In particular, the additive terms in y and z are invariant under a diagonalization of the diabatic Hamiltonian. However, the dynamics is coupled in all directions due to the velocity rescaling (see Eq. (15)) and decoherence scheme (see Eq. (16)). We use system-specific self-consistent units, *i.e.*, we measure energies in units of ϵ , lengths in units of x_0 , and masses in units of m , where the mass of our system is 1 (see Sec. S2.1 † and Table S1 †) for the remainder of this Section. Time is measured in units of $\sqrt{mx_0^2/\epsilon}$.

The diabatic potentials are coupled to each other by a constant coupling of V_c , giving the diabatic Hamiltonian,

$$H(x, y, z) = \begin{pmatrix} V_+(x, y, z) & V_c \\ V_c & V_-(x, y, z) \end{pmatrix}, \quad (20)$$

which upon diagonalization provides the gap g between the corresponding avoiding adiabatic potentials (here labeled as ground and excited states, see Fig. 4a). This model of an avoided crossing is used to compare quantitative and qualitative results against plain brute-force TSH simulations. In this way, we demonstrate that NAFFS yields the correct reaction rate constants and evaluate its computational efficiency. Varying the temperature and the strength of the diabatic coupling gives insight into how these parameters fundamentally condition the transition rate constants.

For the first simulation we use $V_c = 0.4$. This is a rather strong diabatic coupling and leads to a very strongly avoided crossing, *i.e.* the energy gap is $g = 0.8$ (see Fig. 4a), which is large compared to other choices of the coupling constant considered later. Accordingly, one expects very few nonadiabatic surface hops in

the generated trajectories and a dynamics that is predominantly adiabatic in the ground state potential with occasional hops to the excited state. The ground state resembles a one-dimensional double-well potential, where we define the ground state minimum around $x = -1$ as initial region A and the ground state minimum around $x = 1$ as final region B . The two stable regions are separated by a ground state energy barrier of $E_a = 0.64$, see Fig. 4a.

All simulations presented in this Section employ the default TSH decoherence parameter⁶⁴ (see Sec. S2.2 †) and $s = 25$ substeps (see Eq. (10)). The remaining adjustable parameters are the temperature, the time step, and the friction constant. The time step is set to approximately $\Delta t = 0.0539$, such that one oscillation in a ground state minimum consists of at least 20 time steps, and, hence, the dynamics of the system can be adequately captured. The temperature is set to $T \approx 0.2133$, such that the ground state barrier height is $3 k_B T$. This barrier height is sufficiently large to make the barrier crossing a rare event possible and, at the same time, sufficiently low to enable the observation of transition events in brute-force TSH simulations.

The rate constant of a transitions from A to B depends on the friction constant γ that appears in the Langevin equation (see Eq. (17)).⁷⁷ In particular, the rate constant shows a maximum as a function of the friction constant, known as the Kramers turnover.^{77,78} For smaller and larger values of γ the rate constant decreases: at low friction because of slow energy exchange of the system with the environment and at high friction due to slow diffusion at the barrier top. The maximum transition rate constant is expected to occur for a friction constant at which the energy dissipated as the system crosses the barrier is about $1 k_B T$. For a barrier shaped like an inverted parabola, this conditions implies $\gamma_{\max}/m = \omega k_B T/E_a$, where γ_{\max} is the friction constant at which the turnover occurs and ω is the frequency of the unstable mode at the barrier top. For the parameters selected here, the turnover friction is $\gamma_{\max} \approx 0.94$. Hence, the friction coefficient selected for our simulations, $\gamma = 1.4133$, is slightly higher than the turnover friction.

For the brute-force TSH trajectory, we run 5 million time steps, and for the analysis, we define the ground state region $x < -0.5$ as the initial region A , and the ground state region $x > 0.5$ as the final region B . A representative cutout of the TSH trajectory can be seen in Fig. 4b. It shows the typical behavior of a rare event, *i.e.*, it oscillates for a long time in one of the two regions A or B before it undergoes a fast transition to the other region, where it oscillates again. As the diabatic coupling is very large, the crossing is strongly avoided and we expect small nonadiabatic effects. Indeed, the system spends only very short periods of time in the excited state, see orange circles in Fig. 4b. The corresponding reaction rate constant for the transition from the initial region A to the final region B obtained with the brute-force TSH is $(8.25 \pm 0.28) \cdot 10^{-3}$, see Table 1. This result nicely agrees with that obtained by the NAFFS simulation $(8.72 \pm 0.47) \cdot 10^{-3}$, which aside marginal statistical deviations, demonstrates the quantitative accuracy of our implementation. The computational details for the NAFFS simulation are given in Table S2 †.

Figures 4c and 4d show the superimposed transition paths con-

Table 1 Rate constants k_{AB} , number of sampled transition paths, mean transition times, average numbers of hops in adiabatic representation, and the respective standard deviations (std) obtained by brute-force TSH vs. NAFFS simulations on the model featuring an avoided crossing, with a constant coupling of $V_c = 0.4$.

	TSH	NAFFS
rate constant (10^{-3})	8.25 ± 0.28	8.72 ± 0.47
number of transition paths	1073	1805
mean transition time	2.2	2.1
std transition time	2.0	1.0
mean number of hops	0.0298	0.0321
std number of hops	0.2424	0.2515

necting the regions A and B , as obtained from TSH and NAFFS simulations. The mean time that a transition path takes to go from A to B and the average number of hops occurring during the transition paths are also collected in Table 1, together with their corresponding standard deviations. The larger standard deviation for the transition time in TSH compared to NAFFS stems from the overall lower number of transition paths obtained with TSH and some outlying long transition paths among them. The good qualitative and quantitative agreement between NAFFS and TSH values confirms that the NAFFS simulation correctly samples transition paths.

In order to demonstrate the applicability of NAFFS in harsher conditions, we now decrease the temperature, which effectively increases the barrier and thus the rareness of the event. To avoid variations of the rate constant at different temperatures due to the definition of the boundaries of the stable regions A and B , we fix A as $x < -1$ and B as $x > 1$ on the ground state for the remaining simulations on this model. We expect the temperature dependence of calculated rate constants to follow Arrhenius' law,

$$k_{AB} = \nu \exp\left(-\frac{E_a}{k_B T}\right), \quad (21)$$

with prefactor ν . The reaction rate constants obtained with NAFFS, shown in Figure 5a as a function of the inverse temperature, fit Arrhenius' law remarkably well.

Table 2 illustrates the computational efficiency of NAFFS against TSH, showing that the speedup of NAFFS versus TSH increases with the rareness of the transition.

Note that the average number of time steps needed to obtain one NAFFS trajectory depends on the acceptance probabilities for the various interfaces (especially of the last shooting interface where the total number of final transition paths is determined), and, hence, on the choice of the interface placements. This explains that the average number of time steps required to obtain one reactive NAFFS path is always of the same order of magnitude, in stark contrast to the TSH simulations, which require an increasingly larger number of steps with decreasing temperature. Accordingly, for the lowest temperature (largest barrier height $10 k_B T$), NAFFS sampled 876 transition paths in about one million time steps (flux calculation included) whereas TSH sampled only 4 in the same amount of time steps. This implies a speed up of almost 200 in favor of NAFFS, *i.e.*, a sampling acceleration of two orders of magnitude. We note that at this low temperature, an accurate rate constant calculation is no longer possible within

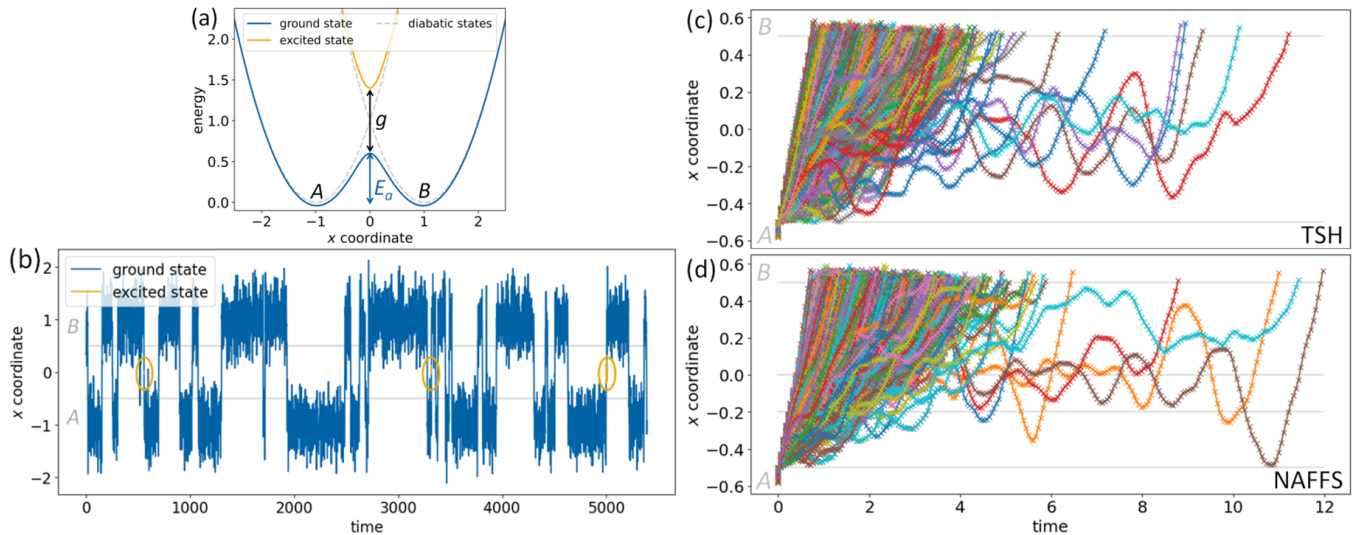


Fig. 4 (a) Analytical model system consisting of two diabatic PESs (dashed lines), coupled by a constant coupling of $V_c = 0.4$. The corresponding adiabatic (ground and excited) states, shown as solid lines, avoid each other by a gap size g . The ground state barrier height is denoted as E_a . (b) Representative cutout of a TSH trajectory propagated in this system as a function of time, where the first snapshot of the cutout is shifted to time zero for convenience. Trajectory parts that are spent in the excited state are shown in orange (and additionally marked by orange ovals) vs. blue in the ground state. The boundaries of the initial and final regions A and B are depicted in gray. (c-d) Superimposed transition paths between the boundaries of the initial and final regions (gray lines) from TSH (c) and NAFFS (d) simulations within this system with $V_c = 0.4$. Different colors allow to discriminate individual transition paths; symbols indicate calculated time steps. The time of the first snapshot of each transition path is set to zero for convenience. The number of plotted transition paths is (c) 1069 (TSH) and (d) 1803 (NAFFS). In the latter case, interfaces are also plotted as gray lines. Note that for a better visualization, we only plot transition paths that are shorter than 12 time units ($> 99.5\%$); this leaves out four events in the case of TSH and two in the case of NAFFS (compare with Table 1).

reason with brute-force TSH, but well feasible with NAFFS.

Table 2 Average number of time steps needed to obtain one transition path in TSH and in NAFFS (flux simulation included) calculations, for different ground state barrier heights E_a (see Fig. 5a). The speedup factor in favour of NAFFS over TSH is also shown.

E_a ($k_B T$)	TSH (time steps)	NAFFS (time steps)	speedup factor
3.0	2464	1083	2.3
4.0	7219	2459	2.9
5.0	16677	1750	9.5
6.0	38889	1120	34.7
10.0	226465	1228	184.4

Finally, since the dynamics with $V_c = 0.4$ is predominantly adiabatic in the ground state potential, we investigate the effect of varying the diabatic coupling from 0.4 to 0.02, thus decreasing the diabatic gap from 0.8 to 0.04, and thus increasing the nonadiabaticity of the avoided crossing. The barrier height in terms of $k_B T$ is kept constant and equal to $4 k_B T$ for all simulations. The rate constant is expected to decrease with smaller gaps, as the nonadiabatic effects increase, *i.e.*, the number of hops in the adiabatic representation increases, and, thus, the probability of a transition for a trajectory that reaches the energy barrier is lower than for systems with higher gap sizes. In other words, with smaller gaps, the nonadiabatic effects become more an obstacle that the system must overcome to complete a transition in addition to the potential energy barrier. In the limit of no diabatic coupling ($V_c = 0$ and, hence, $g = 0$), the system is diabatically trapped, *i.e.*, the dynamics purely evolves on one diabatic state, and the transition rate constant is zero.

As expected, the calculated reaction rate constants are lower

for smaller gap sizes, see Figure 5b. The probability that a trajectory coming from the initial region A hops to the excited state in the vicinity of the barrier, oscillates there for one period and then falls back to the ground state in direction of A due to the inertia, increases with decreasing gap size, *i.e.*, the closer the adiabatic states come to each other. Accordingly, the mean number of surface hops in transition paths also increases with decreasing gap size, see Fig. 5c. We fitted the obtained rate constants (see Fig. 5b) according to the Landau-Zener-type formula^{79–81}

$$k_{AB}(g) = k_{AB}^0 \cdot (1 - e^{-z \cdot g^2}) \quad (22)$$

where k_{AB}^0 is the ground state transition rate constant, and z is a fitting parameter. This expression approximately describes the dependence of the reaction rate constant on the gap size.⁷⁷ As shown in Fig. 5b, the fit nicely reproduces our data. Even for small energy gap sizes, and, thus, highly nonadiabatic situations, the NAFFS and TSH simulation rate constants agree (see Fig. S1 †), further validating our method.

4.2 Rare event dynamics through a conical intersection

To examine the application of NAFFS to rare event dynamics in the vicinity of an explicit conical intersection, we consider a model with two coupled diabatic potential energy surfaces,

$$V_{11}(x, y) = a(x - c)^2 + b(y - d)^2 + ez^2 \quad (23)$$

and

$$V_{22}(x, y) = b(x - d)^2 + a(y - c)^2 + ez^2 \quad (24)$$

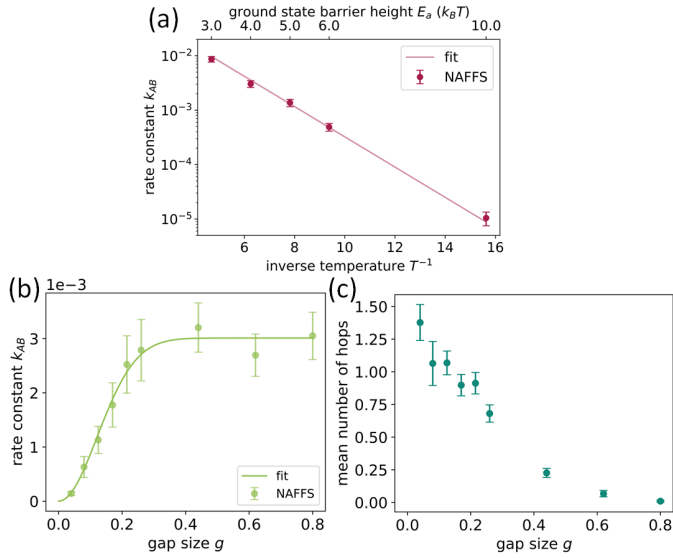


Fig. 5 (a) Rate constant k_{AB} of the model system shown in Fig. 4a with $g = 0.8$ as a function of the inverse temperature. The scale on the top shows the corresponding barrier height in units of $k_B T$. The linear fit takes only the intercept as a fitting parameter, yielding $\nu = 0.19$ (see Eq. (21)). Error bars are plotted as 2σ confidence intervals. (b) Rate constant k_{AB} in the system shown in Fig. 4a vs. the adiabatic gap size g obtained from NAFFS calculations. Error bars are plotted as 2σ confidence intervals. The data are fitted according to Eq. (22), yielding $k_{AB}^0 = 3.01 \cdot 10^{-3}$ and $z = 135.72$. (c) Mean number of hops in the adiabatic representation vs. adiabatic gap size as obtained from NAFFS transition paths. The obtained standard deviations of the mean are plotted as error bars.

with Cartesian coordinates x , y , and z and parameters $a = 0.512$, $b = 0.128$, $c = 0.5$, $d = 3.0$, $e = 12.8$. The narrow harmonic potential around the z coordinate allows us to consider the potential energy landscape as a function of two variables, x and y . Again, all values are given in system-specific self-consistent units (see Sec. S2.1 † and Table S1 †) and the mass is $m = 1$. The coupling between the two diabatic PESs is given by

$$V_{12}(x, y) = V_{21}(x, y) = k(x + y - f) \quad (25)$$

with the prefactor $k = 0.0128$, and $f = 2.3$, resulting in the adiabatic PESs shown in Fig. 6a-b.

We choose the default decoherence parameter⁶⁴ (see Sec. S2.3 †) and $s = 25$ substeps (see Eq. (10)). As meaningful parameter values for the propagation using the Langevin thermostat, we choose a time step of 0.1348, a temperature $T \approx 0.6370$, and a friction coefficient $\gamma \approx 0.7995$. In contrast to the model discussed in Sec. 4.1, here the rare event is not due to a high barrier, as this is only $1 k_B T$, but due to a small diabatic coupling that makes the system stay preferably on one *diabatic* surface (*i.e.*, diabatic trapping). Accordingly, the dynamics shows frequent hops between the ground and excited adiabatic PESs in regions close to the conical intersection (see Fig. 6c), *i.e.*, in general twice during a typical oscillation period in one of the minima. Hence, in this case the rare event is a rare hop in the diabatic representation, *i.e.*, a transition between the two diabatic PESs V_{11} and V_{22} (Eq. (23)-(24)). The initial region A and final region B are defined by $(x - y) \geq 2.5$ and $(x - y) \leq -2.5$, respectively, plus the

additional condition that the system needs to be located in the ground state. The stable region's boundaries also correspond to the first and last interface in the NAFFS simulation.

For this model, we performed a plain brute-force TSH simulation of 5 million time steps. The resulting rate constant, $(5.58 \pm 0.13) \cdot 10^{-3}$, for the transition from A to B agrees very well with the rate constant obtained using a NAFFS calculation, $(5.80 \pm 0.30) \cdot 10^{-3}$, performed with 1 million time steps in the flux simulation followed by 2000 shots per interface (see Table 3). Computational details for the NAFFS simulations are given in Table S3 of Sec. S2.2 †. A second NAFFS simulation of half the size of the previous one (0.5 million time steps and 1000 shots per interface, see Sec. S2.3 †) still yields the correct result, namely $k_{AB} = (5.56 \pm 0.41) \cdot 10^{-3}$, highlighting the efficiency of NAFFS.

Table 3 Rate constant k_{AB} , number of sampled reactive paths, average transition times, average number of hops in adiabatic representation, and the respective standard deviations (std) obtained by brute-force TSH vs. NAFFS simulations, for the model with a conical intersection

	TSH	NAFFS
rate constant (10^{-3})	5.58 ± 0.13	5.80 ± 0.30
number of transition paths	1857	1025
mean transition time	87.67	87.98
std transition time	47.30	45.46
mean number of hops	2.89	2.73
std number of hops	2.10	2.13

The transition paths obtained by the NAFFS simulations (Fig. 6d) are very similar to the ones obtained from brute-force TSH simulations (Fig. S2a †), demonstrating that NAFFS correctly samples transition paths in strong nonadiabatic regimes. Therefore, we next change the parameters of our model system to study it under different conditions. First, we investigate the dependence of the reaction rate constant on temperature. As can be seen in Fig. 7a, due to the stronger nonadiabaticity of the system, the dependence is stronger than in the case of the avoided crossing (recall Fig. 5a), *i.e.*, the slope in a $\log(k_{AB})$ vs. T^{-1} plot is steeper than that given by Arrhenius' law (Eq. (21)) with an activation energy that equals the ground state barrier height (see Fig. 7a). Fitting the reaction rate constants with the expression

$$k_{AB} = \nu \exp\left(-\frac{E_{a,\text{eff}}}{k_B T}\right), \quad (26)$$

with constant ν yields an effective activation energy of $E_{a,\text{eff}} = 0.812 \pm 0.036$, which is significantly higher than the ground state energy barrier of $E_a = 0.64$. This means that the nonadiabatic effects lead to an additional barrier that decreases the probability of the system to undergo a transition.

The obtained NAFFS transition paths show the expected qualitative behavior for different temperatures: their distribution is broader for higher temperatures as the system has more energy available, and is narrower for low temperatures where the transition paths are located in the region around the conical intersection. In regions close to the conical intersection, the energy that the system needs to transition to the final region B is lower than in regions far away from the conical intersection, see the narrower distribution of transition paths in Fig. 6e along the $x = y$

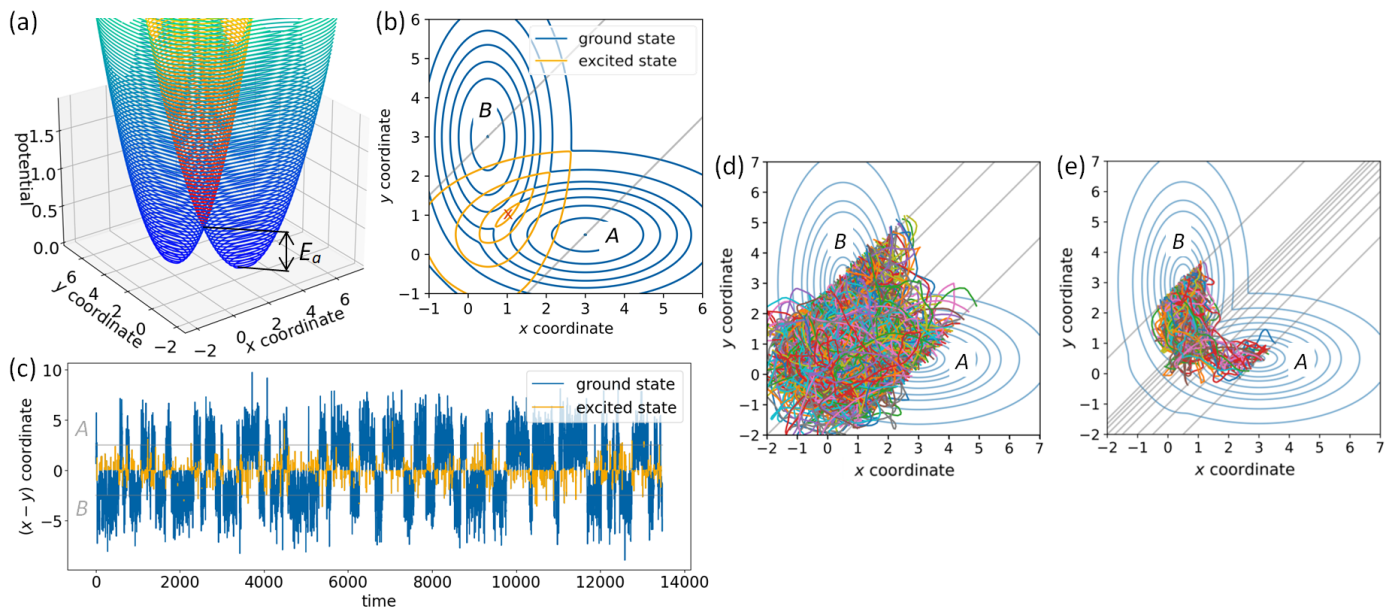


Fig. 6 (a-b) Adiabatic representation of the potential energy landscape of Eq. (23)-(25), shown as a function of x and y as a surface in three dimensions (a) and as a contour plot, where the boundaries of the initial and final regions A and B are shown in gray (b). The ground state is plotted in blue and the excited state in orange. In (b), the location of the conical intersection is marked in red. (c) Representative cutout of a TSH trajectory projected on $(x-y)$ obtained for the model system as a function of time, where the first snapshot of the cutout is shifted to time zero for convenience. For better overview, stable state boundaries are shown in gray. Sojourns in the ground state are plotted in blue, stays in the excited adiabatic state are plotted in orange. (d-e) Transition paths obtained in the NAFFS simulation for temperatures chosen such that the ground state barrier height equals $1 k_B T$ (d) and $6 k_B T$ (e). For the latter the distribution is narrower than for the former, where higher energy regions of the PESs can be visited. Adiabatic ground state contour lines are shown in blue, and interfaces used in the NAFFS simulations in gray.

diagonal direction compared to Fig. 6d. At low temperatures (see Fig. 6e), the rare event is mainly determined by the high potential barrier, whereas for high temperatures (see Fig. 6d), the rareness is predominantly caused by the nonadiabatic effects.

Figure 7b shows that the rate constants of reactive paths that exhibit a given number of hops between the ground and the excited adiabatic PESs differ from each other. In general, the fraction of transition paths that do not undergo hops increases with decreasing temperature, while the fraction of transition paths that feature hops decreases with decreasing temperature (see Fig. S2b †). This is because the system needs energy to undergo hops to the excited state, but has less energy available the lower the temperature is (see Fig. S2d †). Note that due to using velocity rescaling (see Eq. (15)), the number of hops to the excited state might be slightly overestimated, because the system can use all the kinetic energy along the velocity vector to perform a hop. Rescaling along the NAC direction—usually regarded as more accurate⁸²—would lead to fewer upwards hops, because less kinetic energy is usually available along the NAC direction. For simplicity, here we use velocity rescaling.

Since we defined the initial and final regions A and B in the adiabatic ground state, a transition path from A to B can only have an even number of hops in the adiabatic representation. The “hop-dependent” rate constants (see Fig. 7b) are fitted according to Eq. (26), yielding effective activation energies $E_{a,\text{eff}}$ for transition paths with a certain number of hops between the ground and excited adiabatic PESs. $E_{a,\text{eff}}$ increases with increasing number of hops, which again agrees with the necessity to spend energy for

hopping events (see Fig. 7c). The effective activation energy for transition paths showing zero hops, *i.e.*, reaction paths evolving entirely in the ground state, is $E_{a,\text{eff}} = 0.653 \pm 0.043$, which within the range of uncertainty aligns accurately with the ground state energy barrier of $E_a = 0.64$. Hence, transition paths evolving only in the ground state follow Arrhenius’ law even if this ground state is part of a highly nonadiabatic PES landscape. Furthermore, nonadiabatic transition paths also follow approximately Arrhenius’ law, but with a higher effective activation energy. The latter can be understood when thinking about nonadiabatic effects as prolonging the transition path (*e.g.*, because of turning around and having to come back again), which can be compensated by higher energies and hence the reaction barrier seems effectively higher.

An estimate of the computational savings obtained when using our NAFFS implementation is shown in Table 4. As in the case of the rare event dynamics through an avoided crossing (Table 2), here we also achieve a speedup factor of about 200 for the largest barrier height considered.

5 Conclusions

In this work, we have introduced a nonadiabatic forward flux sampling (NAFFS) method that uses the trajectory surface hopping (TSH) algorithm for the underlying dynamics simulation. This method extends the previous fields of application of FFS to capture rare events in electronically excited systems, such as those initiated by the absorption of a photon. NAFFS is therefore suitable to deal with excited-state processes that occur on very

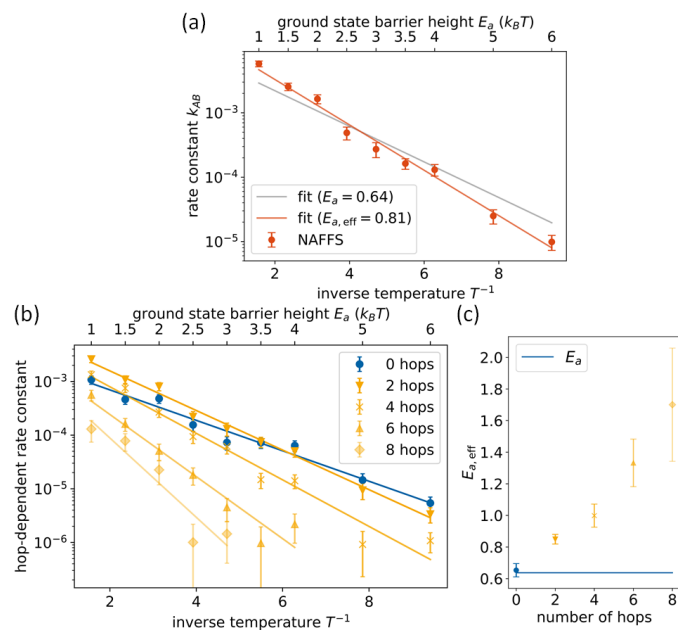


Fig. 7 (a) Rate constant k_{AB} as a function of the inverse temperature (the corresponding ground state barrier in units of $k_B T$ is indicated on the upper axis). Error bars are plotted as 2σ confidence intervals. The data are fitted according to Eq. (26), yielding $E_{a,eff} = 0.812$ and $\nu = 0.017$, and to Eq. (21), yielding $\nu = 0.0079$. (b) Reaction rate constants due to transition paths from A to B that have a certain number of hops, as a function of the temperature. Blue indicates a transition path purely in the adiabatic ground state (zero hops) and orange implies transition paths involving the excited state. The data are fitted according to Eq. (26). Data for more than 8 hops (see Fig. S2c †) are not statistically significant. (c) Effective activation energies as a function of the number of hops. Blue line indicates the ground state energy barrier. Error bars are shown as 2σ confidence intervals.

long time scales, which cannot be otherwise accessed with plain brute-force TSH simulations. Using two models that exemplify different regimes of rareness and nonadiabaticity, we demonstrate that NAFFS produces quantitatively and qualitatively correct results at a computational cost that is two orders of magnitude lower than that of conventional TSH molecular dynamics simulations. Unlike previous efforts to develop nonadiabatic transition path sampling methods,³⁸ our method does not need to propagate trajectories back in time, and, hence, avoids serious problems in long simulations that include several hopping events.^{37,40}

The presented approach is particularly promising to investigate photoinduced chemical reactions that are hindered by potential energy barriers or very small nonadiabatic couplings, and thus take a long time to occur. Exciting examples include DNA damage and repair processes,^{83,84} enone [2+2] photocycloadditions⁸⁵ and many more.

Conflicts of interest

There are no conflicts to declare.

Acknowledgements

The authors thank the University of Vienna for continuous support, in particular the one provided in the framework of the re-

Table 4 Average number of time steps needed in a NAFFS simulation to obtain one reactive path (flux simulation included) and average number of time steps needed in a brute-force TSH simulation to obtain one reactive path, shown for different ground state barrier heights E_a (see Fig. 7a). The speedup factor in favour of NAFFS over TSH is also shown

E_a ($k_B T$)	TSH (time steps)	NAFFS (time steps)	speedup factor
1.0	2865	1165	2.5
1.5	5618	1040	5.4
2.0	12195	837	14.6
2.5	26316	850	31.0
3.0	66667	732	91.1
3.5	66667	1987	33.6
4.0	166667	1495	111.5
5.0	1000000	8460	118.2
6.0	1000000	4968	201.3

search platform ViRAPID. M. X. T., and L. G. appreciate additional support provided by the Austrian Science Fund, W 1232 (MolTag). The computational results presented have been achieved (in part) using the Vienna Scientific Cluster (VSC). The authors thank the SHARC development team, and the ViRAPID members for insightful discussions. We thank Barbara Wagner for her contributions to some NAFFS calculations.

References

- 1 K. Honda, M. Konishi, M. Kawai, A. Yamada, Y. Takahashi, Y. Hoshino and S. Inoue, *Nat. Prod. Commun.*, 2012, **7**, 459–462.
- 2 L. Candish, K. D. Collins, G. C. Cook, J. J. Douglas, A. Gómez-Suárez, A. Jolit and S. Keess, *Chem. Rev.*, 2022, **122**, 2907–2980.
- 3 N. Feliu, E. Neher and W. J. Parak, *Science*, 2018, **359**, 633–635.
- 4 J. P. Holland, M. Gut, S. Klingler, R. Fay and A. Guillou, *Chem. Eur. J.*, 2020, **26**, 33–48.
- 5 *Molecular devices for solar energy conversion and storage*, ed. H. Tian, G. Boschloo and A. Hagfeldt, Springer, Singapore, 2018.
- 6 G. Ciamician, *Science*, 1912, **36**, 385–394.
- 7 *Ultrafast Phenomena in Molecular Sciences: Femtosecond Physics and Chemistry*, ed. R. De Nalda and L. Bañares, Springer International Publishing AG, Cham, 2013.
- 8 *Conical intersections: theory, computation and experiment*, ed. W. Domcke, D. R. Yarkony and H. Köppel, World Scientific, 2011.
- 9 N. J. Turro, *Molecular Photochemistry*, 1965, p. 148.
- 10 E. F. Zwicker, L. I. Grossweiner and N. C. Yang, *J. Am. Chem. Soc.*, 1963, **85**, 2671–2672.
- 11 S. Hammes-Schiffer and J. C. Tully, *J. Chem. Phys.*, 1995, **103**, 8513–8527.
- 12 C. Dellago and P. G. Bolhuis, *Advanced Computer Simulation Approaches for Soft Matter Sciences III. Adv. Polym. Sci.*, Springer, Berlin, Heidelberg, 2009, pp. 167–233.
- 13 *Quantum Chemistry and Dynamics of Excited States: Methods and Applications*, ed. R. Lindh and L. González, John Wiley & Sons, 2020.
- 14 B. F. Curchod and T. J. Martínez, *Chem. Rev.*, 2018, **118**,

- 3305–3336.
- 15 S. Reiter, D. Keefer and R. De Vivie-Riedle, *Quantum Chemistry and Dynamics of Excited States: Methods and Applications*, Wiley & Sons, 2020, ch. 11, pp. 355–381.
- 16 R. Crespo-Otero and M. Barbatti, *Chem. Rev.*, 2018, **118**, 7026–7068.
- 17 S. Mai, P. Marquetand and L. González, *Quantum Chemistry and Dynamics of Excited States: Methods and Applications*, John Wiley & Sons, 2020, ch. 16, pp. 499–530.
- 18 J. P. Zobel, T. Knoll and L. González, *Chem. Sci.*, 2021, **12**, 10791–10801.
- 19 J. Westermayr, M. Gastegger, M. F. Menger, S. Mai, L. González and P. Marquetand, *Chem. Sci.*, 2019, **10**, 8100–8107.
- 20 J. Li, P. Reiser, B. R. Boswell, A. Eberhard, N. Z. Burns, P. Friederich and S. A. Lopez, *Chem. Sci.*, 2021, **12**, 5302–5314.
- 21 J. Westermayr and P. Marquetand, *Mach. Learn.: Sci. Technol.*, 2020, **1**, 043001.
- 22 J. Westermayr and P. Marquetand, *Chem. Rev.*, 2021, **121**, 9873–9926.
- 23 G. Torrie and J. Valleau, *Journal of Computational Physics*, 1977, **23**, 187–199.
- 24 G. Ciccotti and M. Ferrario, *Molecular Simulation*, 2004, **30**, 787–793.
- 25 H. Grubmüller, B. Heymann and P. Tavan, *Science*, 1996, **271**, 997–999.
- 26 A. F. Voter, *Phys. Rev. Lett.*, 1997, **78**, 3908–3911.
- 27 A. K. Faradjian and R. Elber, *The Journal of Chemical Physics*, 2004, **120**, 10880–10889.
- 28 A. Laio and M. Parrinello, *Proceedings of the National Academy of Sciences*, 2002, **99**, 12562–12566.
- 29 W. E, W. Ren and E. Vanden-Eijnden, *Phys. Rev. B*, 2002, **66**, 052301.
- 30 C. Dellago, P. G. Bolhuis, F. S. Csajka and D. Chandler, *J. Chem. Phys.*, 1998, **108**, 1964–1977.
- 31 R. J. Allen, P. B. Warren and P. R. Ten Wolde, *Phys. Rev. Lett.*, 2005, **94**, 018104.
- 32 R. J. Allen, D. Frenkel and P. R. Ten Wolde, *J. Chem. Phys.*, 2006, **124**, 024102.
- 33 R. J. Allen, D. Frenkel and P. R. Ten Wolde, *J. Chem. Phys.*, 2006, **124**, 194111.
- 34 E. Pieri, D. Lahana, A. M. Chang, C. R. Aldaz, K. C. Thompson and T. J. Martínez, *Chem. Sci.*, 2021, **12**, 7294–7307.
- 35 C. Aldaz, J. A. Kammeraad and P. M. Zimmerman, *Phys. Chem. Chem. Phys.*, 2018, **20**, 27394–27405.
- 36 J. O. Lindner, K. Sultangaleeva, M. I. Röhr and R. Mitrić, *J. Chem. Theory Comput.*, 2019, **15**, 3450–3460.
- 37 A. J. Schile and D. T. Limmer, *J. Chem. Phys.*, 2018, **149**, 214109.
- 38 M. C. Sherman and S. A. Corcelli, *J. Chem. Phys.*, 2016, **145**, 034110.
- 39 J. C. Tully, *J. Chem. Phys.*, 1990, **92**, 1061–1071.
- 40 J. E. Subotnik and Y. M. Rhee, *J. Phys. Chem. A*, 2015, **119**, 990–995.
- 41 S. Hammes-Schiffer and J. C. Tully, *The Journal of Chemical Physics*, 1995, **103**, 8528–8537.
- 42 T. S. Van Erp, D. Moroni and P. G. Bolhuis, *J. Chem. Phys.*, 2003, **118**, 7762–7774.
- 43 R. J. Allen, C. Valeriani and P. R. Ten Wolde, *J. Phys.: Condens. Matter*, 2009, **21**, 1–40.
- 44 P. G. Bolhuis and D. W. Swenson, *Adv. Theor. Simul.*, 2021, **4**, 1–14.
- 45 B. Peters, *Annu. Rev. Phys. Chem.*, 2016, **67**, 669–690.
- 46 F. A. Escobedo, E. E. Borrero and J. C. Araque, *J. Phys.: Condens. Matter*, 2009, **21**, 333101.
- 47 D. Berkov, E. K. Semenova and N. L. Gorn, *Phys. Rev. Lett.*, 2021, **127**, 247201.
- 48 E. E. Borrero, M. Weinwurm and C. Dellago, *J. Chem. Phys.*, 2011, **134**, 244118.
- 49 S. Hussain and A. Haji-Akbari, *J. Chem. Phys.*, 2020, **152**, 060901.
- 50 P. G. Bolhuis and C. Dellago, *Eur. Phys. J. Spec. Top.*, 2015, **224**, 2409–2427.
- 51 C. Dellago, P. G. Bolhuis and P. L. Geissler, *Lect. Notes Phys.*, 2006, **703**, 349–391.
- 52 E. E. Borrero and F. A. Escobedo, *J. Chem. Phys.*, 2008, **129**, 024115.
- 53 L. Verlet, *Phys. Rev.*, 1967, **159**, 98–103.
- 54 L. Verlet, *Phys. Rev.*, 1968, **165**, 201–214.
- 55 N. Grønbech-Jensen, N. R. Hayre and O. Farago, *Comput. Phys. Commun.*, 2014, **185**, 524–527.
- 56 M. Richter, P. Marquetand, J. González-Vázquez, I. Sola and L. González, *J. Chem. Theory Comput.*, 2011, **7**, 1253–1258.
- 57 S. Mai, P. Marquetand and L. González, *Int. J. Quantum Chem.*, 2015, **115**, 1215–1231.
- 58 S. Mai, P. Marquetand and L. González, *Wiley Interdiscip. Rev.: Comput. Mol. Sci.*, 2018, **8**, 1–23.
- 59 J. C. Tully and R. K. Preston, *J. Chem. Phys.*, 1971, **55**, 562–572.
- 60 T. R. Nelson, A. J. White, J. A. Bjorgaard, A. E. Sifain, Y. Zhang, B. Nebgen, S. Fernandez-Alberti, D. Mozyrsky, A. E. Roitberg and S. Tretiak, *Chem. Rev.*, 2020, **120**, 2215–2287.
- 61 E. Fabiano, T. W. Keal and W. Thiel, *Chem. Phys.*, 2008, **349**, 334–347.
- 62 F. Plasser, S. Mai, M. Fumanal, E. Gindensperger, C. Daniel and L. González, *J. Chem. Theory Comput.*, 2019, **15**, 5031–5045.
- 63 M. Heindl and L. González, *J. Chem. Phys.*, 2021, **154**, 144102.
- 64 G. Granucci, M. Persico and A. Zocante, *J. Chem. Phys.*, 2010, **133**, 134111.
- 65 N. Grønbech-Jensen and O. Farago, *Mol. Phys.*, 2013, **111**, 983–991.
- 66 D. W. Swenson, J. H. Prinz, F. Noe, J. D. Chodera and P. G. Bolhuis, *J. Chem. Theory Comput.*, 2019, **15**, 813–836.
- 67 D. W. Swenson, J. H. Prinz, F. Noe, J. D. Chodera and P. G.

- Bolhuis, *J. Chem. Theory Comput.*, 2019, **15**, 837–856.
- 68 P. Eastman and V. S. Pande, *Comput. Sci. Eng.*, 2010, **12**, 34–39.
- 69 P. Eastman, M. S. Friedrichs, J. D. Chodera, R. J. Radmer, C. M. Bruns, J. P. Ku, K. A. Beauchamp, T. J. Lane, L. P. Wang, D. Shukla, T. Tye, M. Houston, T. Stich, C. Klein, M. R. Shirts and V. S. Pande, *J. Chem. Theory Comput.*, 2013, **9**, 461–469.
- 70 D. Van Der Spoel, E. Lindahl, B. Hess, G. Groenhof, A. E. Mark and H. J. Berendsen, *J. Comput. Chem.*, 2005, **26**, 1701–1718.
- 71 B. Hess, C. Kutzner, D. Van Der Spoel and E. Lindahl, *J. Chem. Theory Comput.*, 2008, **4**, 435–447.
- 72 J. Westermayr, M. Gastegger and P. Marquetand, *J. Phys. Chem. Lett.*, 2020, **11**, 3828–3834.
- 73 F. Plasser, S. Gómez, M. F. Menger, S. Mai and L. González, *Phys. Chem. Chem. Phys.*, 2019, **21**, 57–69.
- 74 K. T. Schütt, P. J. Kindermans, H. E. Saucedo, S. Chmiela, A. Tkatchenko and K. R. Müller, *Adv. Neural Inf. Process. Syst.*, 2017, **30**, 992–1002.
- 75 K. T. Schütt, H. E. Saucedo, P. J. Kindermans, A. Tkatchenko and K. R. Müller, *J. Chem. Phys.*, 2018, **148**, 241722.
- 76 T. S. van Erp and P. G. Bolhuis, *J. Comput. Phys.*, 2005, **205**, 157–181.
- 77 P. Hänggi, P. Talkner and M. Borkovec, *Rev. Mod. Phys.*, 1990, **62**, 251–341.
- 78 L. Rondin, J. Gieseler, F. Ricci, R. Quidant, C. Dellago and L. Novotny, *Nature Nanotechnology*, 2017, **12**, 1130–1133.
- 79 O. Novaro, M. D. A. Pacheco-Blas and J. H. Pacheco-Sánchez, *Adv. Phys. Chem.*, 2012, **2012**, 720197.
- 80 C. Zener, *Proc. R. Soc. London, Ser. A*, 1932, **137**, 696–702.
- 81 L. D. Landau, *Phys. Z. Sowjetunion*, 1932, **2**, 118.
- 82 J. E. Subotnik, A. Jain, B. Landry, A. Petit, W. Ouyang and N. Bellonzi, *Annu. Rev. Phys. Chem.*, 2016, **67**, 387–417.
- 83 M. Barbatti, A. Borin and S. Ullrich, *Photoinduced Phenomena in Nucleic Acids I and II*, Springer, Cham, Topics in Current Chemistry edn, 2015, vol. 355 and 356.
- 84 R. Improta, F. Santoro and L. Blancafort, *Chem. Rev.*, 2016, **116**, 3540–3593.
- 85 R. Brimiouille and T. Bach, *Science*, 2013, **342**, 840–843.

Supporting Information: Nonadiabatic forward flux sampling for excited-state rare events

Madlen Maria Reiner,^{ab} Brigitta Bachmair,^{ac} Maximilian Xaver Tiefenbacher,^{ac} Sebastian Mai,^d Leticia González,^{*ad} Philipp Marquetand,^{*ad} and Christoph Dellago^{*ae}

Contents

S1 Implementation details	1
S1.1 OPS (Open Path Sampling)	1
S1.2 SHARC (Surface Hopping including ARbitrary Couplings)	1
S1.3 PySHARC (Python wrapper of SHARC)	1
S1.4 SchNarc (Interface between SchNet and SHARC)	1
S2 Analytical model systems	2
S2.1 Reduced unit systems	2
S2.2 Rare event dynamics through an avoided crossing	2
S2.3 Rare event dynamics through a conical intersection	2

S1 Implementation details

S1.1 OPS (Open Path Sampling)

The modified OPS^{1,2} version used in this work includes engines for SHARC³ and SchNarc⁴, and an optimized engine for SchNarc called SchNarcOpt. Furthermore, we add a path simulator called `forward_flux`, containing different versions of FFS (forward flux sampling)⁵ algorithms, in particular a general one applicable to any engine, and optimized versions dedicated to the SchNarcOpt engine. The latter include a general one and one that can be restarted at each interface. The code is available at <https://github.com/MadlenReiner/openpathsampling/tree/virapid>.

S1.2 SHARC (Surface Hopping including ARbitrary Couplings)

We include a Langevin thermostat^{6,7} in the SHARC program. The SHARC code including our modifications is available upon request and will be made publicly available in a forthcoming release.

S1.3 PySHARC (Python wrapper of SHARC)

PySHARC is an interface used to perform SHARC simulations in a Python program. We modified the function `run_sharc` within the class `SHARC_INTERFACE` so that it is possible to execute single time steps instead of a whole SHARC trajectory. The modified version of the code is available on request and will also be made publicly available in a forthcoming release of SHARC.

S1.4 SchNarc (Interface between SchNet and SHARC)

SchNarc⁴ is originally designed as an interface between SHARC and an extension to excited-state properties of the neural network potential package SchNet.^{8,9} The module `schnarc_md.py` is modified to incorporate the analytical models. Exam-

^a Research Platform on Accelerating Photoreaction Discovery (ViRAPID), University of Vienna, Währinger Straße 17, 1090 Vienna, Austria. E-mail: leticia.gonzalez@univie.ac.at, philipp.marquetand@univie.ac.at, christoph.dellago@univie.ac.at

^b Vienna Doctoral School in Physics, University of Vienna, Boltzmannngasse 5, 1090 Vienna, Austria.

^c Vienna Doctoral School in Chemistry, University of Vienna, Währinger Straße 42, 1090 Vienna, Austria.

^d Institute of Theoretical Chemistry, Faculty of Chemistry, University of Vienna, Währinger Straße 17, 1090 Vienna, Austria.

^e Faculty of Physics, University of Vienna, Kolingasse 14-16, 1090 Vienna, Austria.

Table S1 Unit conversion table for the analytical model systems between conventional units and system-specific self-consistent units used in this work

	Model system “avoided crossing”	Model system “conical intersection”
energy E	$[E] = 1 \varepsilon \hat{=} 0.05 \text{ Ha}$	$[E] = 1 \varepsilon \hat{=} 0.078125 \text{ Ha}$
length L	$[L] = 1 x_0 \hat{=} 1 \text{ Bohr}$	$[L] = 1 x_0 \hat{=} 1 \text{ Bohr}$
mass M	$[M] = 1 m \hat{\approx} 1837.15 m_e$	$[m] = 1 m \hat{\approx} 1837.15 m_e$
time t	$[t] = 1 \sqrt{\frac{mx_0^2}{\varepsilon}} \hat{\approx} 4.6366 \text{ fs}$	$[t] = 1 \sqrt{\frac{mx_0^2}{\varepsilon}} \hat{=} 3.7093 \text{ fs}$
temperature T	$[T] = 1 \frac{\varepsilon}{k_B} \hat{\approx} 15788.76 \text{ K}$	$[T] = 1 \frac{\varepsilon}{k_B} \hat{\approx} 24669.93 \text{ K}$
Planck’s constant \hbar	$\hbar \approx 0.1043379668 \sqrt{\varepsilon mx_0^2}$	$\hbar \approx 0.0834703735 \sqrt{\varepsilon mx_0^2}$

ples for the models discussed in the paper are provided at <https://github.com/MadlenReiner/SchNarc/tree/virapid/src/scripts>.

S2 Analytical model systems

S2.1 Reduced unit systems

Since our models are analytically constructed, using conventional units like femtoseconds for times or electron volts for energies is not the best solution, because it may suggest connections to real chemical systems that do not exist. Therefore, we decided to convert our results to system-specific units that are meaningful for the respective analytical models and that are internally consistent, *i.e.*, comparable relative to each other within each system of units.

For the model featuring an avoided crossing (see Sec. 4.1), we choose our energy unit $\hat{=} 1 \varepsilon$ and length unit x_0 such that the diabatic potential energy surfaces in x are defined as

$$V_{\pm} = \frac{\varepsilon}{x_0^2} (x - x_0)^2 \quad (1)$$

i.e., the two diabatic PESs have minima at $x = \pm 1 x_0$ and intersect the y axis at 1ε . Masses are measured in units of the mass m of the system. Times are measured in units of $\sqrt{\frac{mx_0^2}{\varepsilon}}$. The unit of action in our unit system is $\sqrt{\varepsilon mx_0^2}$. The temperature in a conventional unit system is accessed via the relation $\frac{k_B T}{\varepsilon} = 1$.

For the model featuring a conical intersection (see Sec. 4.2), we choose energy, length, time, and mass units of our unit system in the same manner, by placing our diabatic PESs minima at coordinates $(x, y) = (0.5 x_0, 3.0 x_0)$ and $(x, y) = (3.0 x_0, 0.5 x_0)$, and fixing one energy unit ε as intersect of the diabatic potentials and the z axis.

The final conversion table between the unit system used by SHARC input files (*i.e.*, atomic units for everything except for time that is measured in femtoseconds) and the unit systems used for the analytical model systems are shown in Table S1.

S2.2 Rare event dynamics through an avoided crossing

The time step used in this model system is 0.25 fs in conventional units. We use a TSH decoherence parameter $C = 2$, which in atomic units corresponds to 0.1 Ha.¹⁰ Computational details for the NAFFS simulation given in Table 1 in our paper are shown in Table S2. For the NAFFS simulation of half the size that is mentioned in the paper, we use 0.5 million time steps in the flux calculation and 1000 shots per interface, and the definition of the interfaces is not changed compared to Table S2.

Brute-force TSH results accompanying Fig. 5b in our paper are shown in green in Fig. S1. They agree very well with our NAFFS results.

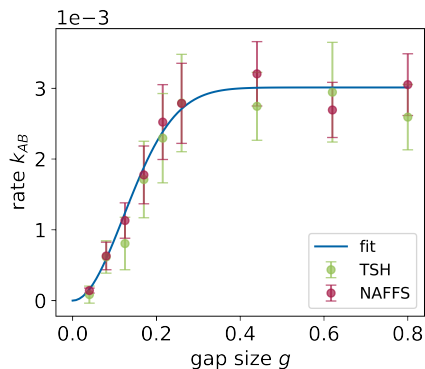
S2.3 Rare event dynamics through a conical intersection

The time step used in this model system is 0.5 fs in conventional units. We use a decoherence parameter $C = 1.28$, which in atomic units corresponds to 0.1 Ha.¹⁰

Computational details for the NAFFS simulation given in Table 3 in our paper are shown in Table S3

Table S2 Computational details for the NAFFS simulation presented in Table 1 in our paper.

flux sim.	time steps	crossing events	flux (10^{-3})
	1 million	2137	(77.1 ± 1.7)
NAFFS sim.	interfaces in x	shots per interface	crossing prob.
	$-0.5 \rightarrow -0.2$	2000	(24.6 ± 1.0)%
	$-0.2 \rightarrow 0.0$	2000	(50.9 ± 1.2)%
	$0.0 \rightarrow 0.5$	2000	(90.25 ± 0.67)%

**Fig. S1** Brute-force TSH rates as a function of the gap size g compared to Fig. 5b in our paper.

For qualitative comparison of the reactive paths of the TSH and NAFFS comparisons presented in our work, we show here (see Fig. S2a) the transition paths obtained in the TSH simulation consisting of 5 million time steps that is described in the paper (see Sec. 4.2). They qualitatively agree with the ones sampled in the NAFFS simulation, which are shown in Fig. 6d in our paper. Note that almost twice as many reactive paths are plotted in case of the TSH simulation (1857, see Fig. S2a) than by the NAFFS simulation (1025, see Fig. 6d in the paper), resulting in the TSH paths being denser. Note that the initial and final regions A and B are defined not only geometrically as plotted in Fig. S2a, but also in terms of the PES, namely on the ground state. Accordingly, paths that seem to sojourn in A or B in the plot are located on the excited state – and, hence, neither in A nor in B .

An evaluation of the average number of hops in transition paths as a function of the inverse temperature shows a decreasing behavior (see Fig. S2b). In accordance to that we find that the fraction of paths which undergo the transition purely on the ground state with respect to the total number of reactive paths increases with decreasing temperature, whereas the ratio of transition paths that show hops to the excited state decreases with decreasing temperature (see Fig. S2c). Fig. S2 also shows the ratio of reactive paths that have more than eight hops in a transition. Only in the three calculations with the highest temperatures this fraction is greater than zero. Where such hops occur, their number is very small (only 29 hops in all calculations combined), both of which militate against examining these numbers in more detail statistically as they are not significant, so we limit ourselves to the paths that show eight hops or fewer.

Fig. S2d shows the mean energy of a hop from the ground state to the excited state as a function of the inverse temperature. It is obtained as the potential energy difference at the geometries where the hops occur. As expected, it decreases with decreasing temperature, since energy must be spent for hops, and the system has less energy available at a lower temperature. At higher temperature, both hops that require a lot of energy and those that cost little energy can occur, while at low temperature, only those hops that require little energy are possible. Accordingly, the standard deviation of the mean energy decreases with decreasing temperature.

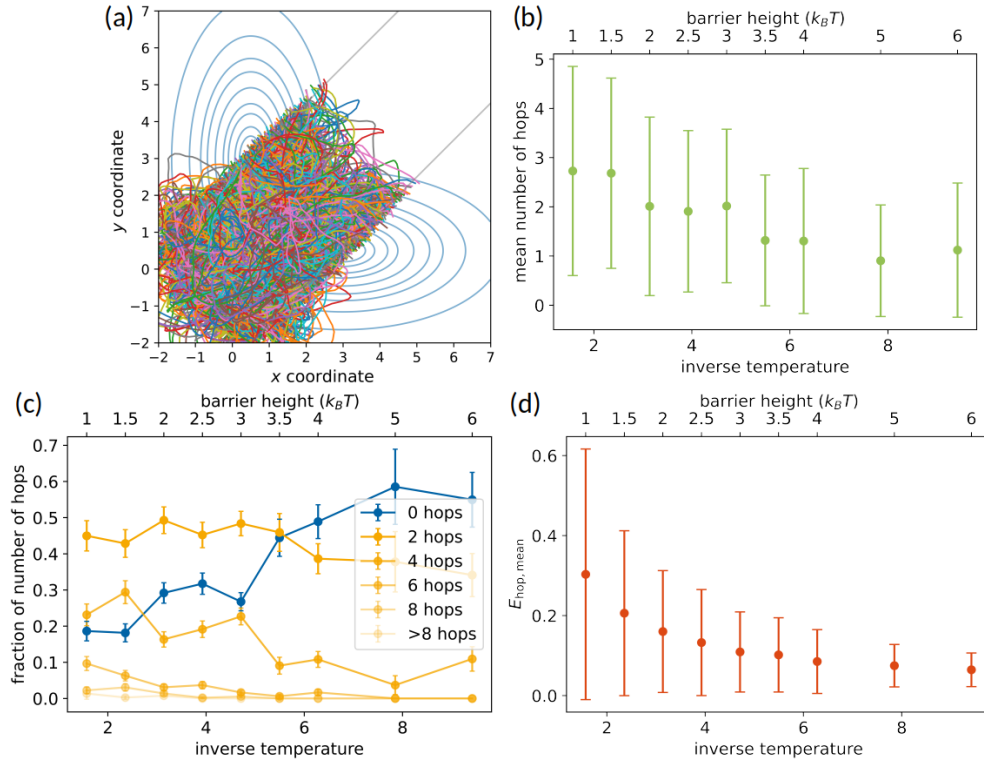


Fig. S2 (a) 1857 transition paths obtained in the TSH simulation of the two-dimensional analytical model. Adiabatic ground state contour lines are shown in blue, and the boundaries of the initial and final regions are shown in gray. (b) The mean number of hops per NAFFS transition path as a function of the inverse temperature, and, alternatively, as a function of the barrier height. The error bars show the obtained standard deviation and do not indicate the accuracy of the obtained results. (c) The ratio of NAFFS transition paths showing a certain number of hops, where the x axes are the same as in (b). The values of the error bars Δf are calculated with respect to the number of paths N showing the specific number of hops and their ratio f with respect to the total number of transition paths, *i.e.*, $\Delta f = f \cdot \frac{\sqrt{N}}{N}$. (d) The average potential energy of a hop from the ground state to the excited state in a TSH simulation, where the x axes equal the ones in (b). The error bars indicate the obtained standard deviation.

Table S3 Computational details for the NAFFS simulation presented in Table 3 in the main paper.

flux sim.	time steps	crossing events	flux (10^{-3})
	1 million	6527	(100.1 ± 2.8)
NAFFS sim.	interfaces in $(x - y)$	shots per interface	crossing prob.
	2.5 \rightarrow 0.0	2000	(29.9 ± 1.1)%
	0.0 \rightarrow -1.5	2000	(37.8 ± 1.1)%
	-1.5 \rightarrow -2.5	2000	(51.3 ± 1.2)%

References

- 1 D. W. Swenson, J. H. Prinz, F. Noe, J. D. Chodera and P. G. Bolhuis, *Journal of Chemical Theory and Computation*, 2019, **15**, 813–836.
- 2 D. W. Swenson, J. H. Prinz, F. Noe, J. D. Chodera and P. G. Bolhuis, *Journal of Chemical Theory and Computation*, 2019, **15**, 837–856.
- 3 S. Mai, M. Richter, M. Heindl, M. F. Menger, A. Atkins, M. Ruckebauer, F. Plasser, L. M. Ibele, S. Kropf, M. Oppel, P. Marquetand and L. González, *SHARC 2.1: Surface Hopping Including Arbitrary Couplings – Program Package for Non-Adiabatic Dynamics*, 2019, sharc-md.org.
- 4 J. Westermayr, M. Gastegger and P. Marquetand, *The Journal of Physical Chemistry Letters*, 2020, **11**, 3828–3834.
- 5 R. J. Allen, P. B. Warren and P. R. Ten Wolde, *Physical Review Letters*, 2005, **94**, 018104.
- 6 N. Grønbech-Jensen and O. Farago, *Molecular Physics*, 2013, **111**, 983–991.
- 7 N. Grønbech-Jensen, N. R. Hayre and O. Farago, *Computer Physics Communications*, 2014, **185**, 524–527.
- 8 K. T. Schütt, P. J. Kindermans, H. E. Saucedo, S. Chmiela, A. Tkatchenko and K. R. Müller, *Advances in Neural Information Processing Systems*, 2017, **30**, 992–1002.
- 9 K. T. Schütt, H. E. Saucedo, P. J. Kindermans, A. Tkatchenko and K. R. Müller, *Journal of Chemical Physics*, 2018, **148**, 241722.
- 10 G. Granucci, M. Persico and A. Zocante, *J. Chem. Phys.*, 2010, **133**, 134111.